ASME Journal of Vibration and Acoustics
Online journal at:
https://asmedigitalcollection.asme.org/vibrationacoustics

Nonminimum-Phase-Based Loop Shaping for Multimode Active Damping Control: Application to Piezoelectric Nanopositioning System

Aditya Natu[1]
Precision and Microsystems Engineering,
Faculty of Mechanical Engineering,
Delft University of Technology,
Mekelweg 2,
Delft 2628 CD, The Netherlands
e-mail: A.M.Natu@tudelft.nl

Hassan HosseinNia
Associate Professor
Precision and Microsystems Engineering, Faculty
of Mechanical Engineering,
Delft University of Technology,
Mekelweg 2,
Delft 2628 CD, The Netherlands
e-mail: S.H.HosseinNiaKani@tudelft.nl

Piezoelectric nanopositioning systems, typically guided by flexure mechanisms, are limited by lightly damped resonances, which constrain achievable closed-loop bandwidth. Active damping controllers (ADCs) are widely employed to suppress the dominant first mode and increase bandwidth; however, their effectiveness degrades significantly in the presence of delay, and dominant higher-order modes often remain insufficiently attenuated, further restricting precision. This article proposes a simple loop-shaping methodology that incorporates a constant-gain nonminimum-phase (NMP) filter in series with a linear damping controller. The NMP filter is tuned using two open-loop crossover frequencies to enforce sufficiently large and approximately symmetric phase margins, thereby mitigating delay-induced degradation in closed-loop damping performance. The methodology is further extended to a parallel damping control structure that enables simultaneous suppression of both the first dominant and higher-order modes. Experimental validation on a piezoelectric nanopositioner demonstrates the effectiveness of the proposed strategy, achieving up to 13.7 dB attenuation of higher-order resonances under significant delay. In combination with a standard proportional-integral (PI) motion controller and a nonminimum-phase resonant controller (NRC) targeting the first mode, the overall control architecture extends the closed-loop bandwidth to 760 Hz, surpassing the system's first resonance frequency without compromising low-frequency dynamics.
[DOI: 10.1115/1.4072016]

Keywords: active vibration and noise control, damping, mechatronics and electromechanical systems, structural dynamics and control, system identification, active damping control, delay, nonminimum-phase, loop shaping, piezoelectric nanopositioning

1 Introduction

Nanopositioning systems are widely used in applications requiring subnanometer precision motion control [1], including atomic force microscopy (AFM) probe positioning [2–4], semiconductor alignment and autofocusing [5–7], and life-science micromanipulation [8–10]. These systems are typically driven by piezoelectric actuators, offering large blocking force, fast response, high bandwidth, and compact form factor [8]. Motion guidance is conventionally realized using parallel flexures fabricated from low-damping materials [11,12], leading to frequency responses with multiple lightly damped rigid-body and bending resonances, as well as significant phase lag introduced by high-resolution data acquisition, sensor filtering, and actuator-amplifier dynamics [13].

In conventional sensor-based feedback architectures with linear controllers such as proportional-integral (PI), the closed-loop bandwidth is typically limited to a small fraction of the first dominant resonance due to the low-damped peak [14]. Higher-order modes with large magnitude and close spectral proximity further increase sensitivity to high-frequency disturbances and noise, degrading positioning accuracy, a problem exacerbated by payload-induced downward shifts of these modes [15,16]. To mitigate these limitations, active damping control has become a standard approach due to its low-order structure and straightforward tuning [17–19], typically implemented as an inner loop in dual-loop configurations. Established strategies targeting the dominant resonance include positive position feedback (PPF), integral resonant control (IRC), resonant control (RC), positive velocity and position feedback (PVPF), positive acceleration, velocity, and position feedback

[1]Corresponding author.

Contributed by the Technical Committee on Vibration and Sound of ASME for publication in the Journal of Vibration and Acoustics. Manuscript received January 31, 2026; final manuscript received May 14, 2026; published online June 15, 2026. Assoc. Editor: Dan Zhao.

(PAVPF), and nonminimum-phase resonant controller (NRC) [20–29]. While these methods effectively attenuate the first mode and extend bandwidth, influential higher-order modes often persist. Overactuation-based methods address these modes using additional collocated actuator-sensor pairs at the cost of increased complexity [30], whereas more recent high-pass PPF designs suppress higher-order modes in noncollocated systems with promising damping performance [31].

However, as noted earlier, nanopositioning systems often exhibit delays that can be significant even within the frequency range containing the first few dominant modes targeted by active damping controllers. Such delays can severely degrade achievable damping performance and may even lead to instability [32–34]. Moreover, they complicate controller tuning by increasing the effective complexity of the system's model, which must be taken into account when assessing closed-loop stability and performance. Previous studies have addressed this challenge by incorporating time delay into simplified second-order system models to facilitate analytical controller design and tuning for adequate damping. Examples of such delay-compensated approaches include Butterworth-based IRC [35], fractional-order IRC [36], and modified PVPF [37] and PPF schemes [38]. Nevertheless, these delay-compensation strategies frequently result in analytically intricate models that typically consider only the fundamental mode and its associated time delay. Extending such techniques to models that incorporate higher-order system dynamics becomes progressively more challenging. To address this issue, a method that combines linear resonant damping control with an all-pass filter was proposed to locally compensate for phase lag in the vicinity of structural resonances [39]. In this framework, the all-pass filter is tuned to provide phase compensation according to the loop phase at the resonance frequency. Consequently, the attainable phase margins at the lower and higher crossover frequencies are determined by the overall open-loop frequency response. When the open-loop gain is not perfectly symmetric around the resonance frequency, the phase margins on either side of the resonance become unequal. While this strategy ensures stability, this asymmetry may reduce robustness and induce undesirable amplification of the closed-loop response near the resonance.

In contrast, the present work reformulates delay-compensated active damping as a crossover-based loop-shaping methodology, generally applicable for linear minimum-phase damping controllers, where the proposed method determines the filter parameter from two prescribed open-loop crossover frequencies so as to enforce sufficiently large and approximately equal phase margins on both sides of the targeted resonance. This provides a tuning framework that not only preserves stability, but also reduces undesired closed-loop amplification and improves robustness to uncertainty in the estimated resonance frequency and effective delay.

Building on these observations, the main research contributions of this article are as follows:

(1) Development of a general loop-shaping methodology for linear minimum-phase damping controllers, in which a constant-gain nonminimum-phase (NMP) filter is tuned from two prescribed open-loop crossover frequencies rather than from the resonance frequency alone. The resulting single-parameter design enforces sufficiently large and approximately equal phase margins on either side of the targeted resonance, thereby avoiding undesirable closed-loop amplification and improving robustness to uncertainty in the estimated resonance frequency and effective time delay.

(2) Demonstration that the proposed crossover-based NMP loop-shaping methodology can be embedded in a dual-loop motion-control architecture for multimodal damping, where several damping controllers operate in parallel to suppress both the dominant first mode and higher-order resonances. Experimental results on a piezoelectric nanopositioner confirm improved disturbance rejection around higher-order resonances without compromising overall closed-loop bandwidth.

The remainder of this article is organized as follows. Section 2 presents the loop-shaping methodology for state-of-the-art linear active damping controllers. Section 3 extends this methodology by integrating an NMP filter with a linear damping controller to enhance damping performance in the presence of delay and derive the associated stability and tuning guidelines. Section 4 describes the experimental setup and presents the results obtained using the proposed approach. Finally, Sec. 5 provides concluding remarks.

2 Loop Shaping for Active Damping Control

The objectives of the closed-loop control system for active damping can be articulated in the frequency domain by specifying the desired shapes of the closed-loop and open-loop transfer functions. This section extends the loop-shaping methodology as delineated in Ref. [40].

2.1 Loop-Shaping Criterion. Figure 1 illustrates the closed-loop control architecture that incorporates an active damping controller $C_d(s)$ within a negative feedback configuration. The objective of the control system is to attenuate the resonance peak magnitude at the specified system resonance frequency ω_n, while ensuring that other system dynamics remain unaffected.

In Fig. 1, the open-loop transfer function $\mathcal{L}(s)$ is then expressed as

$$\mathcal{L}(s) = G(s)C_d(s) \tag{1}$$

The closed-loop transfer function $\mathcal{S}_{yn}(s)$, mapped from the output disturbance/noise n to the measured output y, is expressed as

$$\mathcal{S}_{yn}(s) = \frac{1}{1 + G(s)C_d(s)} = \frac{1}{1 + \mathcal{L}(s)} \tag{2}$$

The closed-loop transfer function $\mathcal{S}_{xn}(s)$, mapped from the output disturbance/noise n to the performance (real) output x, is expressed as

$$\mathcal{S}_{xn}(s) = \frac{-G(s)C_d(s)}{1 + G(s)C_d(s)} = \mathcal{S}_{yn}(s) - 1 \tag{3}$$

Similarly, the closed-loop transfer function $\mathcal{PS}_{xd}(s)(= \mathcal{PS}_{yd}(s))$, mapped from the input disturbance d to the performance output x (or measured output y), is expressed as

$$\mathcal{PS}_{xd}(s) = \frac{G(s)}{1 + G(s)C_d(s)} = G(s)\mathcal{S}_{yn}(s) \tag{4}$$

The loop-shaping objectives and the guidelines to achieve them are discussed below:

(1) O_1: *Maximizing Active Damping Performance*
The system resonance peak should be damped as much as possible to enable higher control bandwidths and to avoid excessive excitation of disturbances at that frequency. The

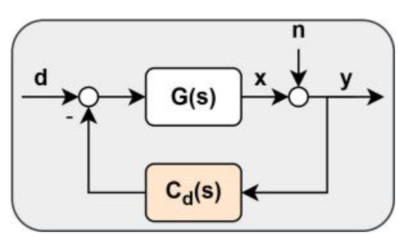

Fig. 1 Feedback control architecture integrating an active damping controller

objective can thus be defined as

$$\max |\mathcal{L}(s)|_{\omega=\omega_n}\Big|\ |\mathcal{PS}_{xd}(s)| \ll |G(s)| \text{ at } \omega = \omega_n \\ \Leftrightarrow |\mathcal{S}_{yn}(s)| \ll 1 \text{ at } \omega = \omega_n \tag{5}$$

(2) *O_2: Maximizing Noise Attenuation Performance*
The system should be able to minimize the influence of high-frequency noise on performance output x, implying good noise attenuation performance. The objective can thus be defined as

$$\min |\mathcal{L}(s)|\ \Big|\ |\mathcal{S}_{xn}(s)| \approx 0 \quad \forall\ \omega \\ \Leftrightarrow |\mathcal{S}_{yn}(s)| \approx 1 \quad \forall\ \omega \tag{6}$$

The conflicting requirements between objectives O_1 and O_2 are evident at $\omega = \omega_n$, where the demand of $\mathcal{S}_{yn}(s) \ll 1$ for active damping opposes the requirement of $\mathcal{S}_{yn}(s) \approx 1$. However, the rationale behind the active damping control requires prioritizing O_1. To reconcile these opposing requirements, the sensitivity function $\mathcal{S}_{yn}(s)$ is ideally designed as a notch filter.

Consequently, the ideal shape of the open-loop function $\mathcal{L}(s)$ results in a triangular form, particularly in proximity to the resonance frequency ω_n where the gain exceeds unity and reaches its maximum, while the shape of the function at other frequencies is subject to the type of damping controller $C_d(s)$ employed. Thus, the gain requirement of the open-loop function $\mathcal{L}(s)$ is established as

$$\begin{aligned} \mathcal{L}(s) &\quad \gg 1 \quad \text{at } \omega \approx \omega_n \\ \mathcal{L}(s) &\quad <1 \quad \forall\ \omega \neq \omega_n \end{aligned} \tag{7}$$

The ideal triangular loop gain results in a region where the gain is above 1, resulting in two crossover frequencies defined as

$$\omega_{c_i} := \{\omega \,|\, \omega \in \mathbb{R} \text{ and } |G(j\omega_{c_i})C_d(j\omega_{c_i})| = 1\}, \quad i = 1, 2 \tag{8}$$

Thus, for the closed-loop stability of the control system, the open-loop has to satisfy the following phase requirements for $k \in \mathbb{Z} \& \omega_{c_1} < \omega_{c_2}$:

$$\begin{aligned} \angle G(j\omega_{c_1})C_d(j\omega_{c_1}) + (2k-1)\pi &\quad \leq 0 \\ \angle G(j\omega_{c_2})C_d(j\omega_{c_2}) + (2k+1)\pi &\quad \geq 0 \end{aligned} \tag{9}$$

2.2 Loop Shaping With Linear Active Damping Controllers. To illustrate these closed-loop and open-loop requirements to fulfill the loop-shaping objectives, a nominal case of a second-order system representing one lightly damped resonance mode is considered, where the system $G(s)$ is given as

$$G_n(s) = \frac{\omega_n^2}{s^2 + 2\zeta_n\omega_n s + \omega_n^2} \tag{10}$$

where ω_n is the resonance frequency of the system and ζ_n represents the damping coefficient.

To conform to the desired open-loop shape, a second-order negative position feedback (NPF) controller with high-pass filter characteristics is adopted as the damping controller, expressed as

$$C_d(s) = \frac{gs^2}{s^2 + 2\zeta_c\omega_c s + \omega_c^2} \tag{11}$$

where ω_c is the corner frequency of the controller tuned at $\omega_c = \omega_n$, and g and ζ_c represent the gain and damping coefficient of the controller.

With such a controller, the design requirements are illustrated in Fig. 2(*b*), where the open-loop transfer function $\mathcal{L}(s) = G_n(s)C_d(s)$ exhibits a triangular shape that provides high gain around ω_n. This results in two phase margins, ϕ_1 and ϕ_2, associated with the two crossover frequencies within the phase band $[-3\pi, -\pi]$. For expository clarity, the loop-shaping principle is initially demonstrated for a single, targeted resonant mode. The underlying rationale generalizes directly to multimode systems by applying the design procedure locally in the neighborhood of each resonance, such that the open-loop gain is shaped to exceed unity in the corresponding frequency region.

Remark 1. Obtaining nearly equal phase margins, that is, $\phi_1 \approx \phi_2$, yields a smoothly damped resonance peak in the closed-loop transfer function $\mathcal{PS}_{yd}(s)$, as shown in Fig. 2(*a*). It should be noted that the level of damping achieved depends on the controller tuning. Specifically, a further reduction in the closed-loop magnitude at ω_n requires either a higher g or a lower ζ_n; however, this comes at the expense of reduced phase margins $\phi_{1,2}$, which in turn affects the closed-loop magnitude at the crossover frequencies $\omega_{c_{1,2}}$.

Remark 2. It should be noted that damping controllers implemented in positive feedback, such as PPF, must be multiplied by -1 to satisfy the stability conditions outlined in Eq. (9). Although controllers with constant low-frequency gain can provide effective damping at the targeted mode, they also introduce undesirable amplification in low-frequency closed-loop dynamics. In contrast, controllers such as NPF, which exhibit high-pass characteristics, can adversely affect systems with uncertain high-frequency dynamics. Ideally, a band-pass-shaped damping controller would address both issues; however, this is beyond the scope of the present work.

3 Loop Shaping With Nonminimum-Phase-Based Delay Compensation

To mitigate the adverse effects of the time delay, this section proposes an NMP filter-based methodology. To illustrate this effect, we consider a second-order lightly damped system with an additional delay term, expressed as

$$G(s) = \frac{\omega_n^2}{s^2 + 2\zeta_n\omega_n s + \omega_n^2} e^{-\tau s} \tag{12}$$

where τ is the time delay in the system.

3.1 Nonminimum-Phase Filter. An NMP filter is expressed by the transfer function:

$$C_n(s) = \left(\frac{s - \omega_d}{s + \omega_d}\right) \tag{13}$$

where ω_d signifies the corner frequency of the filter. A distinctive characteristic of this filter is its constant gain across all frequencies, which is expressed as

$$\left|C_n(j\omega)\right| = 1 \quad \forall\ \omega \in [0, \infty) \tag{14}$$

The phase response of the filter is defined as

$$\angle C_n(j\omega) = -2\tan^{-1}\left(\frac{\omega}{\omega_d}\right) \tag{15}$$

In particular, the phase of the filter transitions from 180 deg to 0 deg as the frequency varies from 0 to $2\omega_d$, and provides the -90 deg phase at ω_d. The filter consists of one pole in the left half-plane at $s = -\omega_d$ and a zero in the right half-plane (RHP) at $s = \omega_d$, resulting in a nonminimum-phase characteristic.

3.2 Nonminimum-Phase Filter-Based Linear Active Damping Control. For the controller defined in Eq. (11) and tuned similarly to the previous case, the closed-loop response $\mathcal{PS}_{yd}(s)$ is shown in Fig. 3(*a*). Although adequate damping is achieved at the targeted resonance frequency ω_n, a pronounced amplification occurs at the second crossover frequency of $\mathcal{L}(s)$. As illustrated in Fig. 3(*b*), this arises because the system delay significantly reduces one of the phase margins, specifically, ϕ_2, to a

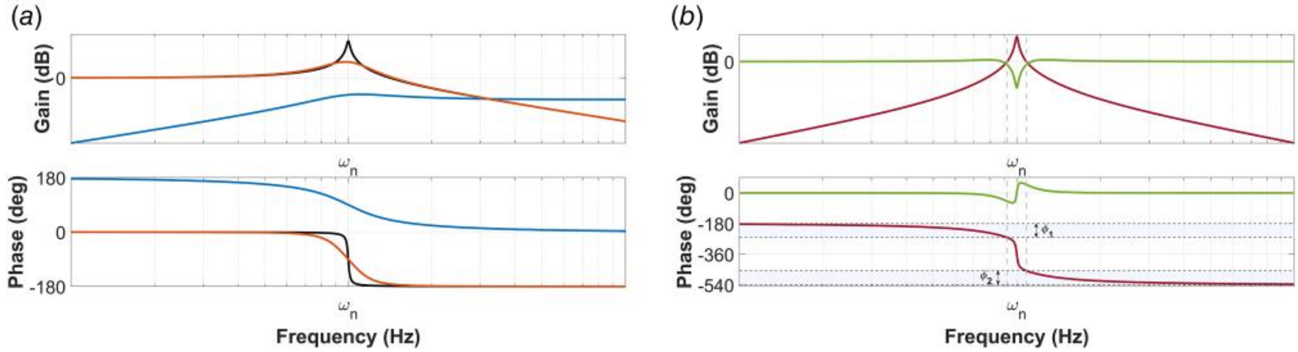

Fig. 2 Frequency response plots: (*a*) system without delay $G_n(s)$ (—), NPF controller $C_d(s)$ (—), and closed-loop function $\mathcal{PS}_{yd}(s)$ (—), (*b*) open-loop function $\mathcal{L}(s) = G(s)C_d(s)$ (—) and closed-loop sensitivity function $\mathcal{S}_{yn}(s)$ (—)

very small value. This reduced phase margin directly causes the observed amplification in the closed-loop response at ω_{c_2}. It should also be noted that larger delays may violate the open-loop phase criterion defined in Eq. (9), resulting in closed-loop instability.

To overcome this limitation, an NMP filter is introduced. Owing to its constant gain and tunable phase characteristics, the NMP filter enables adjustment of the open-loop phase without altering the gain, thereby ensuring adequate values for both phase margins $\phi_{1,2}$. This is achieved by connecting the linear damping controller $C_d(s)$ in series with the NMP filter $C_n(s)$, resulting in the open-loop transfer function, expressed as

$$\mathcal{L}(s) = G(s)C_d(s)C_n(s) \tag{16}$$

Accordingly, the closed-loop transfer function, which characterizes the damping performance, is expressed as

$$\mathcal{PS}_{xd}(s) = \frac{G(s)}{1 + G(s)C_d(s)C_n(s)} \tag{17}$$

The damping controller parameters are tuned to achieve a reasonable peak reduction at ω_n, while the corner frequency of the NMP filter is adjusted to obtain sufficient and preferably equal phase margins ($|\phi_1| \approx |\phi_2|$), thereby ensuring a smoothly attenuated peak in the closed-loop response.

To mitigate spillover effects in the vicinity of the targeted resonance frequency while still achieving adequate attenuation at the resonance mode, it is necessary to ensure sufficiently large phase margins at the relevant crossover frequencies. Inadequate phase margins at these crossover frequencies not only diminish the closed-loop robustness to model uncertainties but also induce pronounced peaks in the closed-loop response at the same frequencies. Consequently, appropriate tuning of the NMP filter frequency ω_d is required so as to guarantee a desired minimum-phase margin $\phi_{\min}$ at the crossover frequencies ω_{c_1} and ω_{c_2}.

To this end, the filter frequency ω_d must satisfy the following inequality:

$$\frac{\omega_{c_2}}{\tan\left(\dfrac{\Xi_2(k)}{2}\right)} \le \omega_d \le \frac{\omega_{c_1}}{\tan\left(\dfrac{\Xi_1(k)}{2}\right)} \tag{18}$$

where

$$\Xi_1(k) = \phi_{\min} + \phi_{d_1} - 2\pi k, \quad \Xi_2(k) = \phi_{d_2} + 2(1-k)\pi - \phi_{\min}$$

ϕ_{d_1} and ϕ_{d_2} denote the open-loop phase in the absence of the NMP filter (i.e., $\arg \mathcal{L}(j\omega_{c_i}) = \arg\left(G(j\omega_{c_i}) \cdot C_d(j\omega_{c_i})\right)$), and k identifies the phase band in which the phase margins reside. The detailed derivation is provided in Appendix A.

In order to enforce equal phase margins, $\phi_1 = \phi_2$, at the two crossover frequencies, the NMP filter frequency ω_d must additionally satisfy

$$\omega_d = \frac{(\omega_{c_1} + \omega_{c_2}) + \sqrt{(\omega_{c_1} + \omega_{c_2})^2 + 4T_k^2\omega_{c_1}\omega_{c_2}}}{2T_k} \tag{19}$$

where $T_k = \tan(B_k)$ and

$$B_k = \frac{\phi_{d_1} + \phi_{d_2} + 2(1-2k)\pi}{2}$$

The detailed derivation is provided in Appendix B.

Remark 3. Spillover can be formalized as unintended frequency regions where the closed-loop disturbance response exceeds the plant response, which can be expressed as

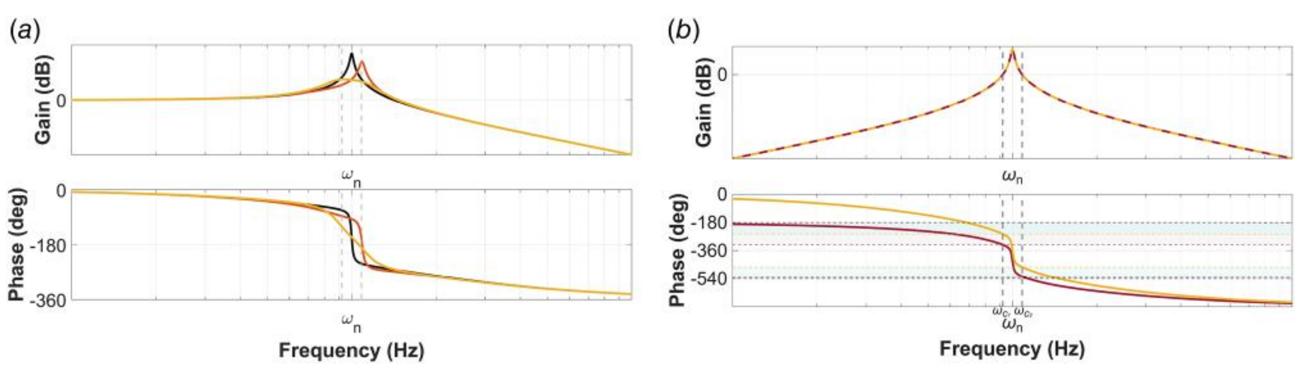

Fig. 3 Frequency response plots: (*a*) system with delay $G(s)$ (—), closed-loop function $\mathcal{PS}_{yd}(s)$(—) with damping controller $C_d(s)$, and closed-loop function $\mathcal{PS}_{yd}(s)$(—) with damping controller $C_d(s)C_n(s)$, (*b*) open-loop function $\mathcal{L}(s) = G(s)C_d(s)$ (—) and open-loop function $\mathcal{L}(s) = G(s)C_d(s)C_n(s)$ (—)

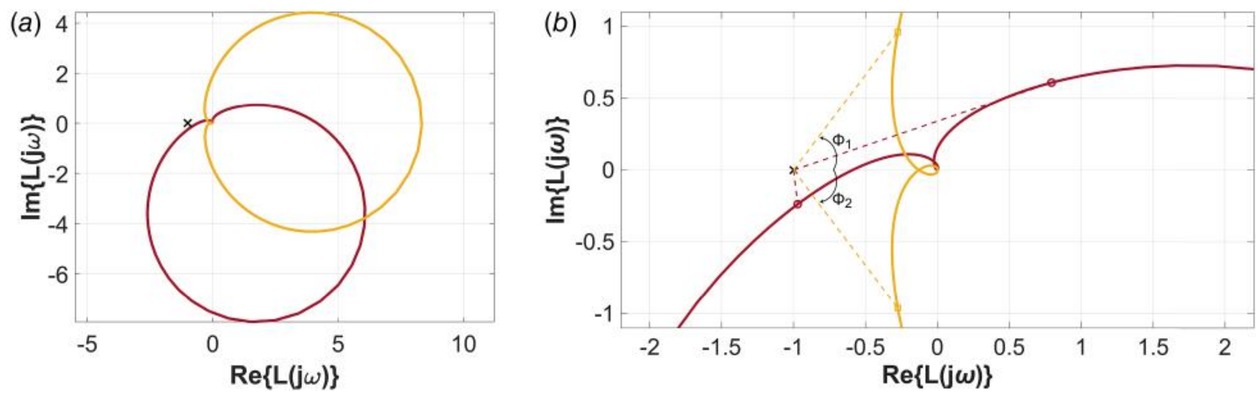

Fig. 4 Nyquist plots: (*a*) open-loop function $\mathcal{L}(s) = G(s)C_d(s)$ (—) and open-loop function $\mathcal{L}(s) = G(s)C_d(s)C_n(s)$ (—) and (*b*) zoomed plot

$|\mathcal{PS}_{xd}(s)| > |G(s)|\ \forall\ \omega$. Thus, spillover is characterized by the condition $|\mathcal{S}_{yn}(s)| > 1\ \forall\ \omega$.

Remark 4. The integer k serves only as a phase-branch index for the two unity-gain crossover points and should not be interpreted as an additional design variable. In Nyquist terms, consecutive phase bands differ only by one full 2π revolution around the critical point -1; thus, they are geometrically equivalent, while k merely keeps track of which wrapped branch is being used to define the phase margins consistently. In practice, k is selected so that both crossover points lie in the same unwrapped phase band $\left[(2k-1)\pi, (2k+1)\pi\right]$, yielding positive generalized phase margins and feasible tuning conditions. For the cases considered here, this typically corresponds to the band $[-3\pi, -\pi]$, i.e., $k=-1$. ∎

Remark 5. Although the NMP filter $C_n(s)$ contains an RHP zero, its effect in the present study is channel-dependent. For the disturbance-rejection transfer function $\mathcal{PS}_{xd}(s) = G(s)/(1+G(s)C_d(s)C_n(s))$, the RHP zero of $C_n(s)$ does not manifest as a zero of $\mathcal{PS}_{xd}(s)$. Its influence arises exclusively through the shared closed-loop denominator, via pole relocation and the associated modification of the phase margin. The improvement in disturbance rejection demonstrated in this work is therefore achieved through phase shaping rather than gain modification. In contrast, for the noise-related channel $\mathcal{S}_{xn}(s) = -((G(s)C_d(s)C_n(s))/(1+G(s)C_d(s)C_n(s)))$, the factor $C_n(s)$ appears explicitly in the numerator, thus inducing its RHP zero in this channel. A comprehensive analysis of the consequences for $\mathcal{S}_{xn}(s)$ and for internal control-effort channels is deferred to future research. ∎

3.3 Loop Shaping for Active Damping With Nonminimum-Phase Filter.

To demonstrate the necessity of the NMP filter, we again consider the case of damping the resonance of a second-order lightly damped system with time delay, as defined in Eq. (12). Two scenarios are compared for active damping control: (a) employing only a linear damping controller $C_d(s)$, as in the previous cases, and (b) employing a series connection of $C_d(s)$ with the NMP filter $C_n(s)$, resulting in the effective controller $C_d(s)C_n(s)$.

With appropriate tuning, the closed-loop damping performance for both cases in the presence of delay is shown in Fig. 3(*a*). It can be seen that the degradation caused by the delay when only $C_d(s)$ is used is effectively mitigated when the NMP filter is introduced. The underlying mechanism is illustrated in Fig. 3(*b*), where the NMP filter introduces a 180 deg phase shift at low frequencies and provides a tunable phase shift around the crossover frequencies via its corner frequency ω_d. This ensures sufficiently large phase margins ($|\phi_{1,2}| \geq 60$ deg). The effect is further clarified in the Nyquist plot in Fig. 4, which shows that the NMP filter produces a frequency-dependent rotation of the open-loop function $\mathcal{L}(s)$ without changing its magnitude, thus restoring the required phase margins. This rotational effect results from the constant-gain property of the filter, with the amount of rotation determined by the frequency-dependent phase shift governed by ω_d.

Thus, for a set x representing the controller parameters of $C_d(s)$, the general objective can be formulated as a mathematical optimization expressed as

$$\begin{aligned}
&\min_{x,\ \omega_d\ \in\ \mathbb{R}^+} \quad |\mathcal{PS}_{xd}(j\omega_n)| + \||\phi_1| - |\phi_2\| \\
&\text{subject to:} \\
&\angle G(j\omega_{c_1})C_d(j\omega_{c_1})C_n(j\omega_{c_1}) + (2k-1)\pi \leq 0 \\
&\angle G(j\omega_{c_2})C_d(j\omega_{c_2})C_n(j\omega_{c_2}) + (2k+1)\pi \geq 0
\end{aligned} \tag{20}$$

The controller tuning procedure is summarized, and general guidelines are provided, as illustrated in Fig. 5.

Remark 6. For certain choices of controller parameters, it may be possible to tune $C_d(s)$ so that sufficient phase margins $\phi_{1,2}$ are achieved even in the presence of delay. However, this significantly complicates the tuning process, and the guidelines commonly reported in the literature may no longer be directly applicable. In practice, the challenge becomes more pronounced as the delay increases around the target frequencies. By employing a series connection of $C_d(s)$ and $C_n(s)$, the tuning procedure is simplified: $C_d(s)$ can be tuned to achieve high-gain at the targeted resonance mode, following established rules for the delay-free system dynamics, while the NMP filter $C_n(s)$ can then be adjusted based on the actual system delay using the proposed open-loop-shaping methodology. Importantly, this technique also enables a stable closed-loop response in scenarios where a purely linear damping controller may lead to instability due to large delays. ∎

3.4 Robustness to System Uncertainties.

In practice, the estimated system frequency response may deviate from the true dynamics due to variations in operating conditions and imperfections in system identification. Tuning damping controllers in the presence of delay requires reasonably accurate knowledge of both the targeted resonance and the effective time delay in the loop. While some degradation of the closed-loop performance is inevitable under such uncertainties, the extent of this degradation is governed by the robustness provided by the control design.

As highlighted in Sec. 1, enforcing approximately equal phase margins at the open-loop crossover frequencies is crucial for avoiding undesired amplification at these frequencies in the closed-loop response and for improving tolerance to model uncertainties. This property constitutes the main distinguishing feature of the proposed method compared with the approach in Ref. [39]. For damping controllers that produce an almost ideal triangular open-loop shape, the crossover frequencies are nearly symmetric about the targeted resonance, and both tuning methods yield comparable closed-loop

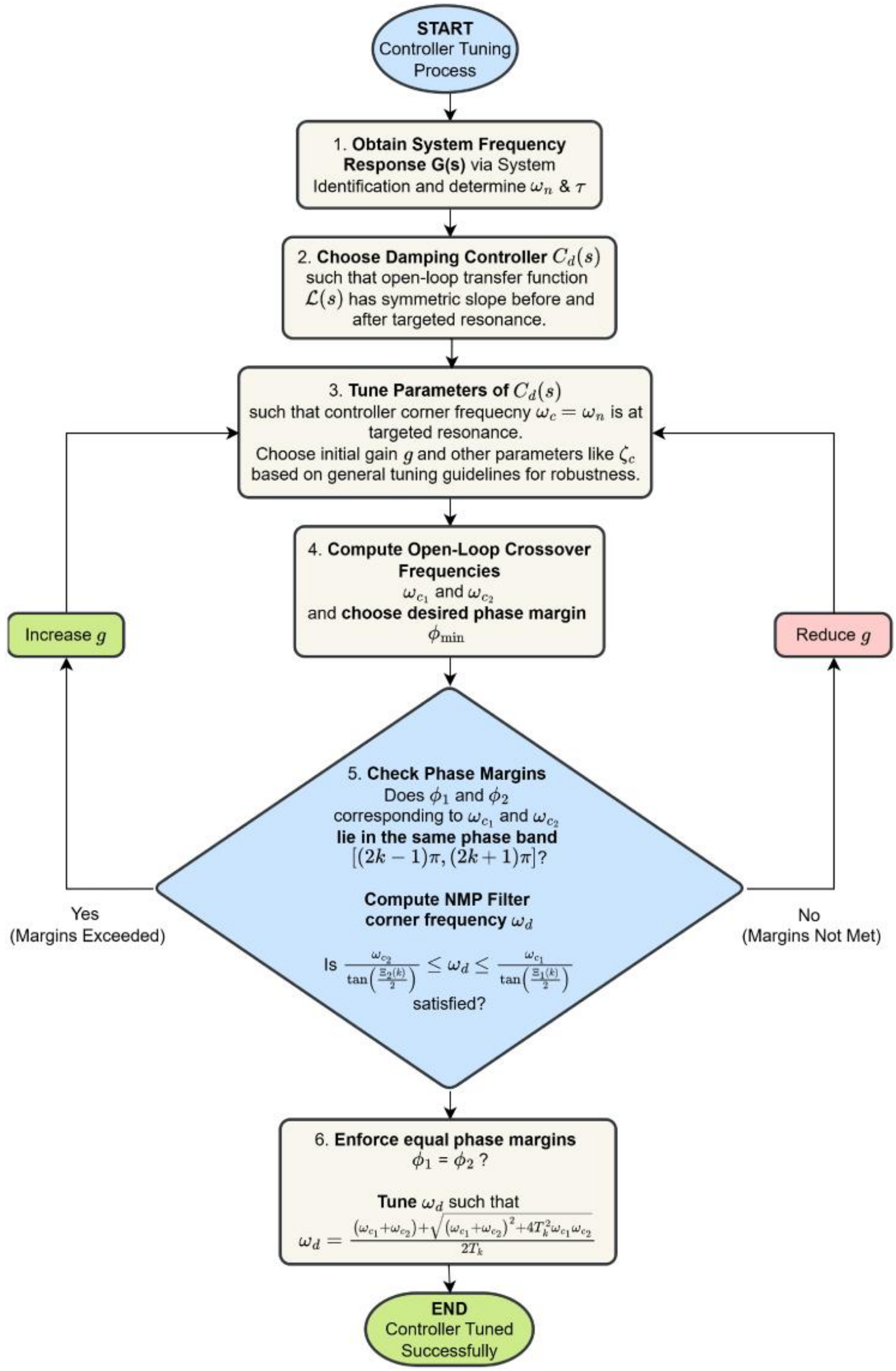

Fig. 5 Controller tuning guidelines based on proposed loop-shaping methodology

behavior. However, for controllers such as PPF that do not enforce such symmetry, the crossover frequencies become asymmetric. In that case, the resonance-based tuning of Ref. [39] naturally leads to unequal phase margins, with one margin significantly smaller than the other (subject to controller gain), which in turn induces amplified closed-loop dynamics near the corresponding crossover frequency. This effect is further exacerbated in the presence of uncertainties in either the estimated resonance frequency or the effective time delay, making the phase margins more sensitive.

To assess the robustness of the system to such uncertainties and to compare the proposed method with Ref. [39], a numerical robustness analysis is performed. Uncertainties are introduced in the estimated system resonance as $\omega_n(1+\delta)$ and in the estimated system delay as $\omega_g(1+\delta)$, where ω_g is derived from a first-order Padé approximation of the delay. To accentuate the impact of crossover asymmetry, a second-order PPF controller is employed. As illustrated in Fig. 6, the closed-loop variations obtained with the NMP filter tuned using the proposed crossover-based method are significantly smaller than those obtained with the resonance-based tuning of Ref. [39] for both types of uncertainty. This improvement stems from the fact that the proposed method ensures symmetric phase margins for the nominal system, thereby reducing the

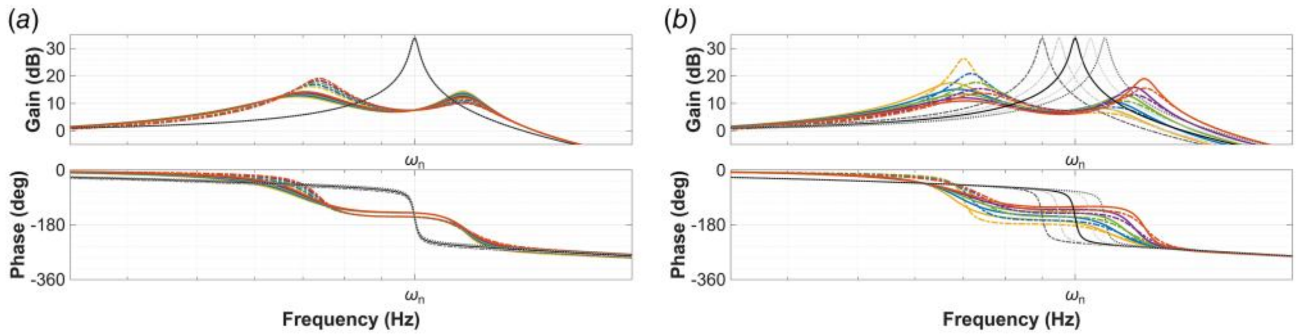

Fig. 6 Closed-loop frequency response plots: (*a*) uncertainty in estimated system delay and (*b*) uncertainty in estimated system resonance. The robustness analysis compares our proposed method (solid colored lines) with the tuning method proposed by Kim and Brennan [39] (dashed-dotted colored lines), and the uncertain system (black/gray lines). The uncertainty cases are as follows: $\delta = -10\%$ (—), $\delta = -5\%$ (—), $\delta = 0\%$ (—), $\delta = +5\%$ (—), and $\delta = +10\%$ (—).

sensitivity of the closed-loop response to perturbations that otherwise create large discrepancies between the phase margins at the two crossover frequencies.

To quantitatively compare robustness under uncertainty, the ratios of the H_∞ and H_2 norms of the closed-loop transfer function relative to those of the plant are reported in Table 1. For comparable damping levels achieved at resonance by both methods, these metrics provide complementary information: the H_∞-norm ratio reflects the worst-case closed-loop amplification over frequency, whereas the H_2-norm ratio captures the overall energy of the closed-loop response and thus provides an aggregate measure of performance across the frequency spectrum.

4 Experimental Setup and Results

This section presents the industrial piezoelectric nanopositioning system employed as an experimental setup to experimentally validate the damping performance attained through the application of the proposed NMP filter-based loop-shaping method.

4.1 System Description. Presented in Fig. 7, the experimental setup utilizes a commercial P-621.1CD PIHera linear precision nanopositioner with a travel range of 100 μm. The single-axis positioning stage incorporates a ceramic-insulated multilayer piezo-stack actuator, a flexure-based mechanism-guided platform, and a high-resolution capacitive sensor. The stage utilizes a voltage amplifier and sensor signal conditioning modules integrated within the modular E-712 piezo-controller. The commercial hardware is integrated with an NI CompactRio chassis with an embedded FPGA, facilitating actuation signals and control for external control. The chassis includes 16-bit analog input–output modules that enable transmission and reception of signals to implement the control approach. The control scheme is implemented using the NI LABVIEW software, which interfaces the host computer and the nanopositioner. The actuation voltage ranges from 0 to 10 V, and the sampling time t_s of the FPGA-based control loop is set to 30 μs.

4.2 System Identification. A sinusoidal chirp signal (0–0.1 V) was generated in LABVIEW and applied to the piezo-actuator for system identification. The resulting displacement was measured using a capacitive sensor, and the input–output data were imported into MATLAB for analysis. Transfer functions were estimated using the MATLAB Signal Processing Toolbox. A high sampling frequency of $F_s = 33.3$ kHz ensured sufficient resolution for accurate identification. A payload of approximately 15 g was mounted on the stage during system identification to accentuate the presence of higher-order modes. The dominant first resonance peak occurs at $\omega_n = 485$ Hz, followed by a significant second mode at $\omega_2 = 2138$ Hz (see Fig. 8(*a*)). A noticeable phase delay of about 0.22 ms is estimated, which results in an additional phase lag of about 38 deg around ω_n and about 110 deg around ω_2, arising from actuator-amplifier dynamics and inherent system delay. Additional higher-order modes of smaller magnitude appear around and beyond 2500 Hz. The observed pole-zero interlacing confirms the collocated nature of the system.

The identified plant model is represented as a rational transfer function with delay, of the form given in Eq. (21), where the identified polynomial coefficients and delay are summarized in Table 2.

$$G(s) = \frac{\sum_{i=0}^{m} b_i s^i}{\sum_{j=0}^{n} a_j s^j} \cdot e^{-\tau s} \tag{21}$$

4.3 Control Architecture. A dual closed-loop control framework is implemented, as illustrated in Fig. 8(*b*). The inner loop comprises active damping controllers $C_{d_{1,2}}(s)$ that mitigate dominant resonance modes, while the outer loop comprises a motion controller $C_t(s)$. The loops operate in conjunction to attenuate resonance modes and enable high bandwidths, facilitating precise reference tracking and effective disturbance rejection. The inner loop integrates two damping controllers in a parallel configuration, with the primary controller aimed at suppressing the dominant resonance peak at 485 Hz and the secondary controller addressing the

Table 1 Comparison of closed-loop norm ratios under delay and resonance uncertainties

	Uncertainty in estimated delay				Uncertainty in resonance frequency			
	Proposed		Existing		Proposed		Existing	
δ (%)	$\frac{\Vert\mathcal{PS}_{xd}(s)\Vert_\infty}{\Vert G(s)\Vert_\infty}$	$\frac{\Vert\mathcal{PS}_{xd}(s)\Vert_2}{\Vert G(s)\Vert_2}$	$\frac{\Vert\mathcal{PS}_{xd}(s)\Vert_\infty}{\Vert G(s)\Vert_\infty}$	$\frac{\Vert\mathcal{PS}_{xd}(s)\Vert_2}{\Vert G(s)\Vert_2}$	$\frac{\Vert\mathcal{PS}_{xd}(s)\Vert_\infty}{\Vert G(s)\Vert_\infty}$	$\frac{\Vert\mathcal{PS}_{xd}(s)\Vert_2}{\Vert G(s)\Vert_2}$	$\frac{\Vert\mathcal{PS}_{xd}(s)\Vert_\infty}{\Vert G(s)\Vert_\infty}$	$\frac{\Vert\mathcal{PS}_{xd}(s)\Vert_2}{\Vert G(s)\Vert_2}$
−10	0.10469	0.35925	0.12888	0.37977	0.15055	0.39486	0.41748	0.60210
−5	0.096583	0.35734	0.14008	0.38728	0.11448	0.36389	0.22170	0.45330
0	0.093291	0.35695	0.15228	0.39620	0.093291	0.35695	0.15228	0.39620
+5	0.09813	0.35771	0.16562	0.40644	0.12435	0.37072	0.11738	0.37638
+10	0.10310	0.35938	0.18026	0.41795	0.17857	0.40725	0.11978	0.38054

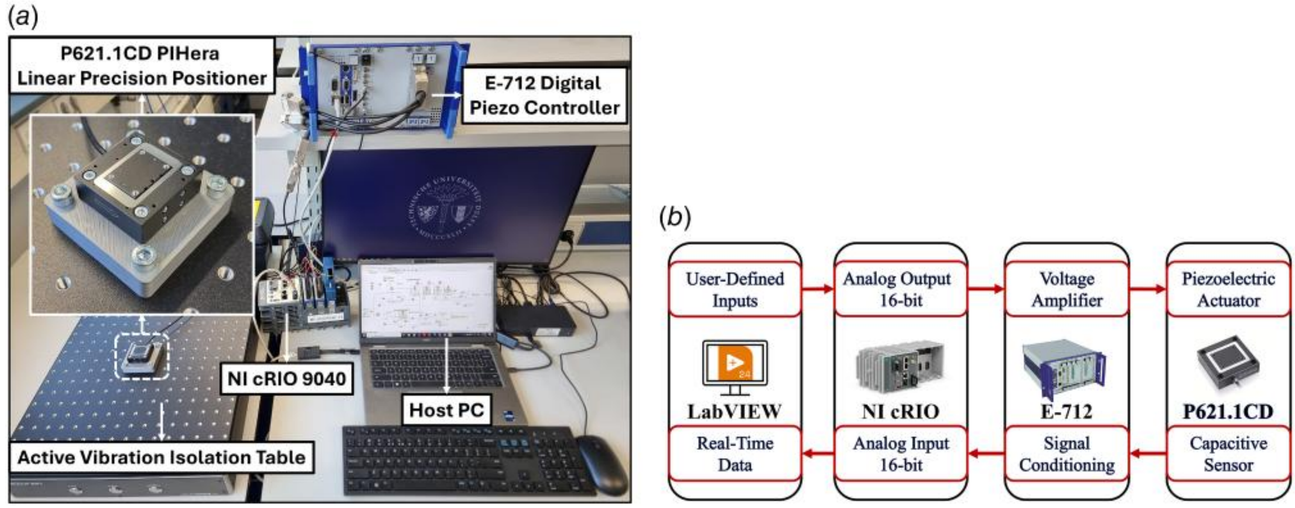

Fig. 7 Experimental setup of a piezo-actuated nanopositioning system: (*a*) experimental platform and (*b*) system workflow

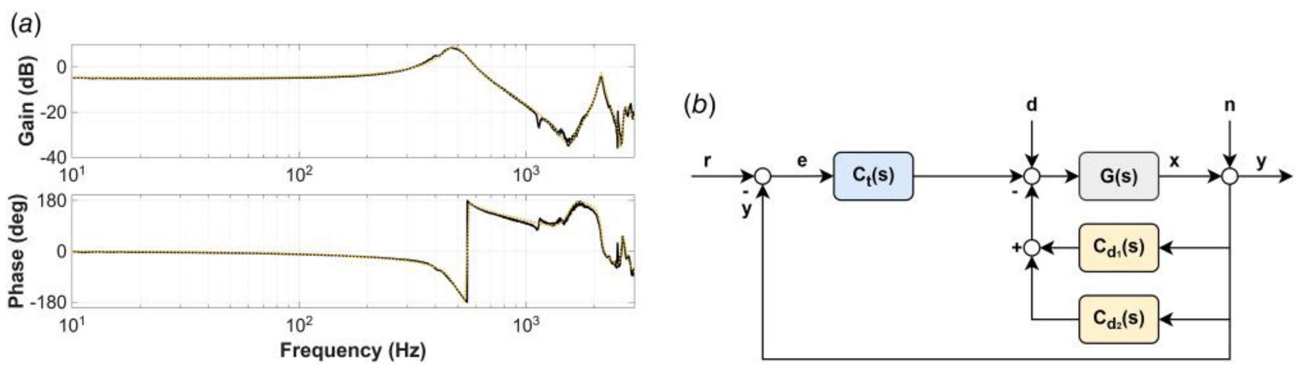

Fig. 8 (*a*) Experimental frequency response plots of system *G*(*s*): experimental identification (—) and estimated transfer function (···), and (*b*) dual closed-loop control architecture incorporating active damping control in parallel configuration

significant higher-order mode at 2138 Hz. This parallel configuration enables straightforward tuning of each controller, using the identified frequency response of the system. Thus, the effective damping controller $C_d(s)$ becomes

$$C_d(s) = C_{d_1}(s) + C_{d_2}(s) \tag{22}$$

For this architecture, the dual closed-loop transfer function $T_{yr}(s)$, mapped from the reference input r to measured output y, corresponding to reference-tracking performance, is expressed as

$$T_{yr}(s) = \frac{G(s)C_t(s)}{1 + G(s)(C_t(s) + C_d(s))} \tag{23}$$

Table 2 Coefficients of the estimated plant transfer function model

Power of s	Numerator coefficient b_i	Denominator coefficient a_i
8	–	1
7	–	3.598×10^4
6	–	7.804×10^8
5	4.057×10^{11}	1.765×10^{13}
4	3.229×10^{15}	1.871×10^{17}
3	1.516×10^{20}	2.157×10^{21}
2	1.085×10^{24}	1.448×10^{25}
1	1.115×10^{28}	2.515×10^{28}
0	6.376×10^{31}	1.109×10^{32}
Time delay τ (s)		2.2×10^{-4}

Similarly, the dual closed-loop transfer function $PS_{yd}(s)$, mapped from the input disturbance d to the performance output x, corresponding to the disturbance-rejection performance, is expressed as

$$PS_{yd}(s) = \frac{G(s)}{1 + G(s)(C_t(s) + C_d(s))} \tag{24}$$

4.4 Closed-Loop Targeting First Resonant Dynamics. As highlighted in Sec. 1, the first lightly damped resonance of the system is the primary limitation to achieving high closed-loop bandwidths. To address this, a damping controller $C_{d_1}(s)$ is first implemented to suppress the resonance peak. In this study, an NRC is employed for three main reasons: (1) it effectively suppresses the resonance peak, (2) it provides high low-frequency gain, which is beneficial for motion-control loop shaping, and (3) when used in conjunction with standard motion-tracking controllers such as PI, it enables high closed-loop bandwidths up to or beyond the first resonance frequency. The NRC is defined as

$$C_{d_1}(s) = k \cdot \left(\frac{s - \omega_a}{s + \omega_a}\right) \tag{25}$$

where k is the controller gain and ω_a is the corner frequency, tuned as $\omega_a = n\omega_n$.

For motion control in the outer feedback loop, a conventional PI controller in series with a first-order low-pass filter is employed:

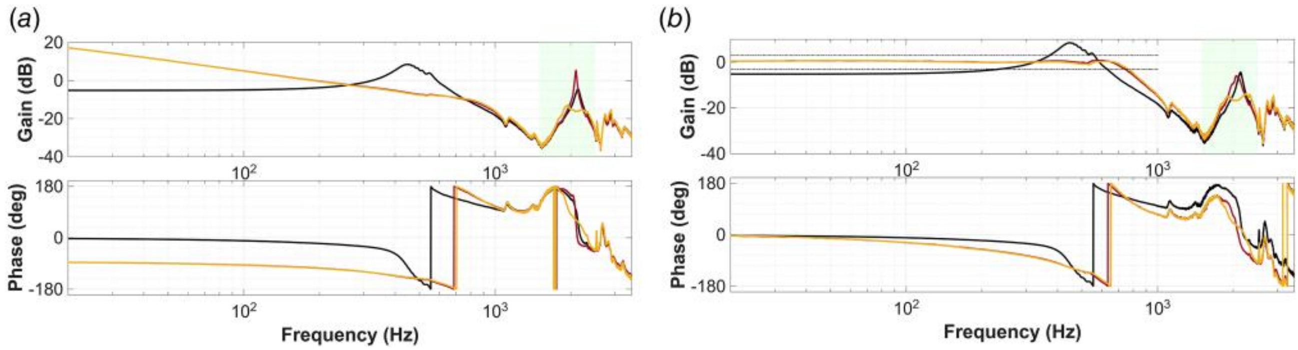

Fig. 9 Experimental frequency response plots: (*a*) identified system *G*(*s*) (—), inner closed-loop response $\mathcal{PS}_{yd}(s)$ with $C_{d_1}(s)$ (—) and with $C_{d_1}(s) + C_{d_2}(s)$ (—), (*b*) identified system *G*(*s*) (—), and dual closed-loop response $T_{yr}(s)$ with $C_{d_1}(s)$ (—) and with $C_{d_1}(s) + C_{d_2}(s)$ (—)

$$C_t(s) = \underbrace{k_p \cdot \left(1 + \frac{\omega_i}{s}\right)}_{\substack{\text{Proportional} \\ \text{integral term}}} \cdot \underbrace{\left(\frac{\omega_l}{s + \omega_l}\right)}_{\substack{\text{Low-pass} \\ \text{Filter}}} \tag{26}$$

where k_p is the proportional gain, ω_i is the integrator frequency, and ω_l is the low-pass cutoff frequency.

For the system identified in Fig. 8(*a*), the NRC parameters are tuned as $k = 1.8025$ and $n = 3$. The inner closed-loop response with NRC only is shown in Fig. 9(*a*), where both the increased low-frequency gain and the suppression of the first resonance peak are evident. The motion controller $C_t(s)$ is tuned with parameters $k_p = 1.2742$, $\omega_i = 25$ Hz, and $\omega_l = 5000$ Hz. The corresponding dual closed-loop response $T_{yr}(s)$, obtained with $C_d(s) = C_{d_1}(s)$, is illustrated in Fig. 9(*b*). As indicated, the closed-loop bandwidth, defined by the −3 dB crossover frequency, is 742 Hz, which significantly exceeds the first resonance frequency of 485 Hz.

However, it should be noted that the NRC controller adversely affects the second dominant mode by amplifying it due to its constant-gain property. Specifically, the second mode, which initially exhibited a magnitude of −4.32 dB, is amplified to 5.41 dB in the inner closed-loop.

Remark 7. To prevent the amplification of higher-order modes, damping controllers with low-pass characteristics, such as PPF, may be employed. However, the closed-loop bandwidths achievable with such controllers are generally lower than those obtained using NRC. To avoid compromising bandwidth, NRC is adopted in this work, while the issue of amplified higher-order modes is addressed in the next subsubsection.

4.5 Loop Shaping for Damping Higher-Order Mode. As discussed previously, the higher-order mode in the identified system response is quite significant, and its magnitude is further amplified in closed-loop operation due to damping control targeted at the first mode. Suppressing this mode is particularly challenging because of the large time delay present around its resonance frequency, as shown in Fig. 8(*a*). To address this, in this section, an NMP-based linear active damping controller is designed to attenuate the amplified higher-order mode. To minimize any impact on the low-frequency closed-loop dynamics already achieved in the previous subsection, a damping controller with a second-order high-pass characteristic is selected. This controller is applied to the existing inner closed-loop dynamics governed by $C_{d_1}(s)$, yielding a desirable triangular open-loop shape. Following the methodology outlined in Sec. 3, the high-pass filter parameters are tuned to maximize damping performance, and the controller is connected in series with an NMP filter to induce a frequency-dependent rotation of the open-loop Nyquist curve, thus ensuring sufficient phase margins at the two crossover frequencies of the modified open-loop function $\mathcal{L}'(s)$, expressed as

$$\mathcal{L}'(s) = \frac{G(s)}{1 + G(s)C_{d_1}(s)} \cdot C_{d_2}(s) \tag{27}$$

where the damping controller $C_{d_2}(s)$ is expressed as

$$C_{d_2}(s) = \underbrace{\left(\frac{g\omega_c^2 s^2}{s^2 + 2\zeta_c\omega_c s + \omega_c^2}\right)}_{\substack{\text{High-pass} \\ \text{filter}}} \cdot \underbrace{\left(\frac{s - \omega_d}{s + \omega_d}\right)}_{\substack{\text{Nonminimum} \\ \text{-phase filter}}} \tag{28}$$

The controller parameters of $C_{d_2}(s)$ are manually tuned using the estimated frequency response and the tuning guidelines, computed as follows: $g = 10^{-8}$, $\zeta_c = 0.15$, $\omega_c = 2100$ Hz, and $\omega_d = 600$ Hz. The resulting open-loop response and the corresponding Nyquist curve are shown in Figs. 10(*a*) and 10(*b*), respectively. Owing to the effect of the NMP filter, the open-loop phase is shifted to yield sufficient phase margins of $|\phi_1| = 58$ deg and $|\phi_2| = 64$ deg. These high phase margins ensure smooth damping performance, as demonstrated in the inner closed-loop response that incorporates a parallel active damping control $C_d(s) = C_{d_1}(s) + C_{d_2}(s)$, shown in Fig. 9(*a*), where the dominant higher-order mode at 2138 Hz is effectively suppressed.

For the dual closed-loop control architecture depicted in Fig. 8(*b*), the corresponding dual open-loop transfer function is expressed as

$$L_D(s) = G(s)(C_t(s) + C_d(s)) \tag{29}$$

Stability of the dual closed-loop system requires that all 0 dB crossover frequencies of $L_D(s)$ exhibit sufficiently large phase margins ϕ_{m_i}; in practice, $\phi_{m_i} \geq 30$ deg is typically considered adequate to ensure robust performance. Closed-loop stability is further assessed by verifying that the Nyquist contour associated with $L_D(s)$ does not encircle the critical point at −1. The Nyquist plots for both configurations are evaluated and shown in Fig. 11(*a*). It can be observed that, owing to the specifically designed frequency-domain characteristics of the second damping controller, the overall Nyquist locus is only minimally influenced, except in the vicinity of, and at frequencies higher than, the second targeted resonance mode.

Remark 8. The parallel damping architecture increases the controller order as additional modal branches are introduced. In practice, however, this increase is modular, and each targeted mode requires only one additional low-order linear damping branch. Since each branch is tuned locally around a specific resonance and implemented in parallel, the resulting structure remains suitable for real-time embedded control and avoids the complexity of synthesizing centralized high-order controllers. ∎

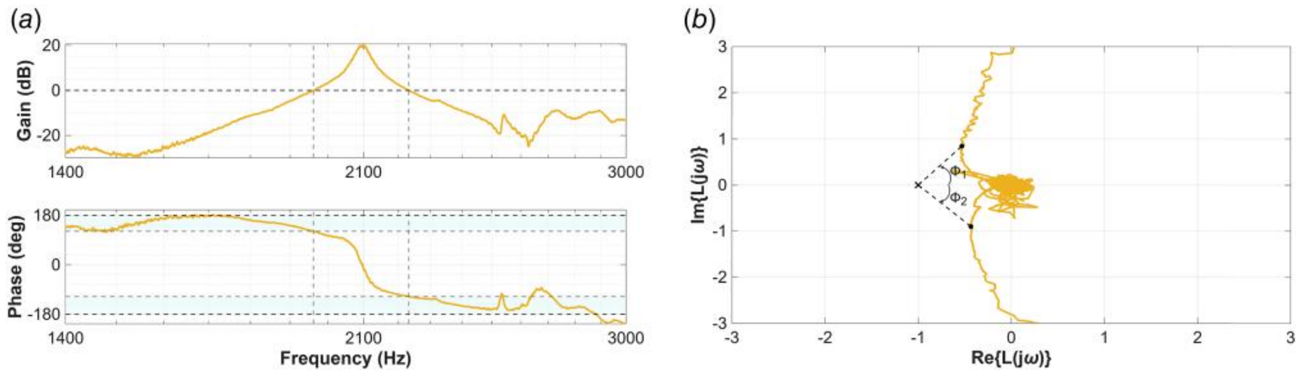

Fig. 10 (*a*) Experimental open-loop frequency response function $\mathcal{L}'(s)$ and (*b*) experimental Nyquist plot of open-loop function $\mathcal{L}'(s)$

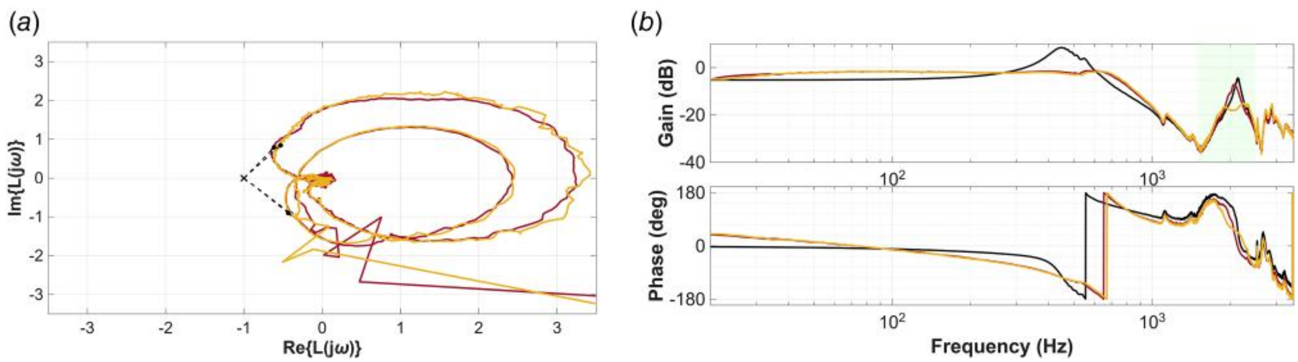

Fig. 11 (*a*) Experimental Nyquist plot of open-loop function $L_D(s)$ with $C_{d_1}(s)$ (—) and with $C_{d_1}(s) + C_{d_2}(s)$ (—), and (*b*) experimental frequency response plots of identified system $G(s)$ (—), dual closed-loop response $PS_{yd}(s)$ with $C_{d_1}(s)$ (—) and with $C_{d_1}(s) + C_{d_2}(s)$ (—)

4.6 Dual Closed-Loop Results. The effect of this parallel damping control in conjunction with motion control is illustrated in the dual closed-loop response $T_{yr}(s)$ in Fig. 9(*b*) and $PS_{yd}(s)$ in Fig. 11(*b*). Compared to the identified plant response, a magnitude reduction of 13.7 dB is achieved in $PS_{yd}(s)$. Furthermore, due to the specifically tailored shape of the controller in the frequency domain, the −3 dB closed-loop bandwidth in $T_{yr}(s)$ is attained at 760 Hz, which remains significantly higher than the system's first resonance frequency.

This result experimentally validates the benefit of employing an NMP filter-based loop-shaping methodology in a parallel damping control architecture, which enables the effective damping of significant higher-order modes, even in the presence of time delay, without compromising the low-frequency closed-loop dynamics.

Disturbance rejection was evaluated using steady-state tracking experiments in which a constant or sinusoidal reference input was applied while a sinusoidal or chirp external disturbance at/around the second resonance frequency (2100 Hz) was injected into the system. To demonstrate the effect of the parallel damping controller on suppressing the higher-order resonance, both cases were tested under identical disturbance conditions. As illustrated in Fig. 12 for a representative case, the sensor-output fluctuations are reduced when the parallel damping controller is employed in

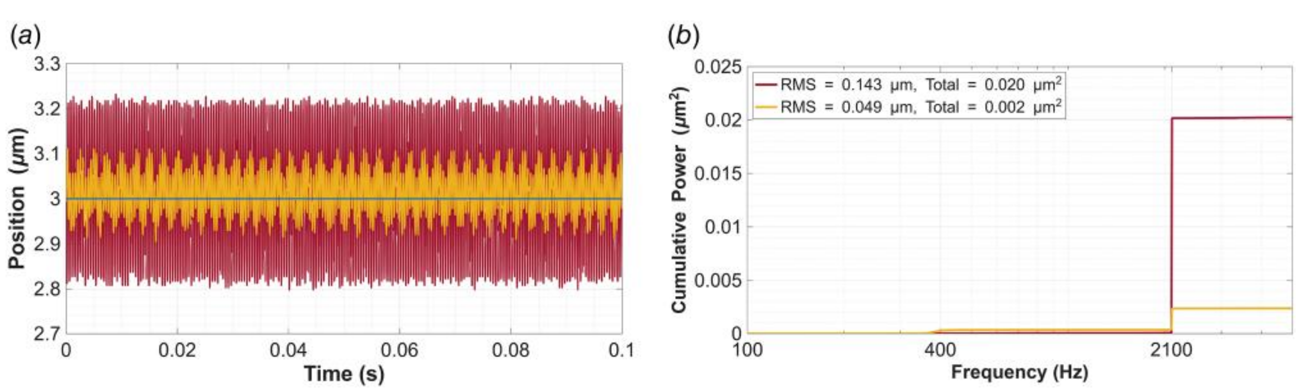

Fig. 12 Comparison of disturbance-rejection performance with $C_{d_1}(s)$ (—) and with $C_{d_1}(s) + C_{d_2}(s)$ (—): (*a*) measured sensor output $y(t)$ and (*b*) its cumulative power spectrum, under a constant reference input (—) and a sinusoidal disturbance at 2100 Hz

Table 3 Dual closed-loop disturbance-rejection performance

Reference signal	Frequency (Hz)	Disturbance signal	Frequency (Hz)	$C_{d_1}(s)$		$C_{d_1}(s) + C_{d_2}(s)$	
				RMS (μm)	Total (μm^2)	RMS (μm)	Total (μm^2)
Constant	–	Sinusoid	2100	0.143	0.020	0.049	0.002
Constant	–	Sinusoidal chirp	2000–2200	0.116	0.014	0.046	0.002
Sinusoid	2100	Sinusoid	2100	0.361	0.130	0.093	0.009

Table 4 Time-domain tracking performance for triangular reference inputs

Frequency (Hz)	$C_{d_1}(s)$		$C_{d_1}(s) + C_{d_2}(s)$	
	$e_{\max}$ (μm)	e_{rms} (μm)	$e_{\max}$ (μm)	e_{rms} (μm)
10	0.10374	0.03613	0.10175	0.03599
20	0.13748	0.06987	0.15205	0.06570
50	0.18937	0.09917	0.18650	0.09924
100	0.16509	0.08473	0.15568	0.08365
150	0.14052	0.05979	0.12778	0.05712
200	0.14095	0.05162	0.11760	0.04600

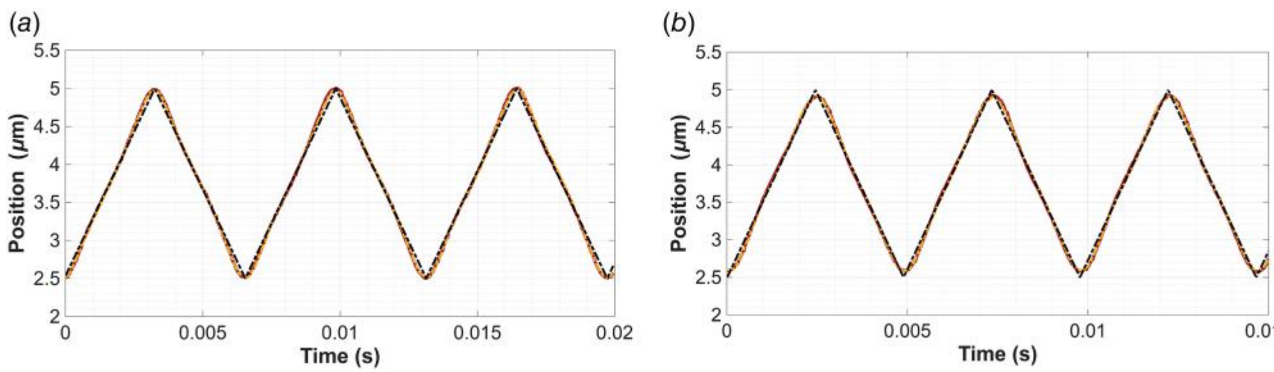

Fig. 13 Comparison of tracking performance for closed-loop function $T_{yr}(s)$ with $C_{d_1}(s)$ (—) and with $C_{d_1}(s) + C_{d_2}(s)$ (- -) with triangular reference (- -) of fundamental frequency: (*a*) 150 Hz and (*b*) 200 Hz

the inner loop, as reported in Table 3. This improvement is further illustrated in the power spectrum, where the cumulative power and corresponding root mean square (RMS) displacement indicate a significant reduction compared to the case without the additional controller. By attenuating the higher-order resonance in the second case, the disturbance propagation is substantially reduced at high frequencies, thereby enhancing the system's positioning precision.

The dual closed-loop reference-tracking performance was evaluated using a triangular reference input representative of raster-scanning operation. Time-domain performance was assessed for triangular inputs with fundamental frequencies ranging from 10 to 200 Hz using two error metrics, namely the root-mean-square tracking error e_{rms} and the maximum tracking error $e_{\max}$. The corresponding results are summarized in Table 4, while Fig. 13 shows two representative examples. It is observed that both control configurations provide comparable tracking performance over the considered frequency range, while the configuration including the parallel damping controller for the higher-order mode yields a slight improvement. This improvement is attributed to the reduced excitation of the higher-order resonance by the higher harmonics inherently present in the triangular reference signal. These results confirm that the inclusion of the additional parallel damping branch for higher-order mode suppression does not compromise the low-frequency closed-loop dynamics and preserves, or slightly improves, the practical reference-tracking performance.

5 Conclusion

This article reformulates delay-compensated active damping as a loop-shaping problem, which is generally applicable to linear damping controllers. A constant-gain NMP filter is tuned from two prescribed open-loop crossover frequencies such that sufficiently large and approximately symmetric phase margins are enforced on either side of the targeted resonance. This single-parameter tuning strategy yields robust closed-loop damping behavior without undesirable gain amplification in the vicinity of the resonance and improves tolerance to modeling uncertainties in both the resonance frequency and the effective time delay. This method can be easily extended to multiple modes in the system response.

The proposed methodology was embedded in a dual-loop motion-control architecture and applied to multimodal damping on a piezoelectric nanopositioner, where parallel damping controllers enable the simultaneous suppression of both the dominant first mode and the dominant higher-order resonance. Experimental results confirmed that damping higher-order modes using the proposed NMP filter-based design improves disturbance rejection around the corresponding resonances without compromising overall closed-loop bandwidth.

Although the method introduces a nonminimum-phase zero in the closed loop, no adverse effects were observed in the present study. A more detailed analysis of the influence of this zero on closed-loop performance will be conducted. Future work will explore the extension of the approach to more complex damping structures and multi-axis platforms operating under variable payloads.

Acknowledgment

This work was financed by Physik Instrumente (PI) SE & Co. KG and cofinanced by Holland High Tech with PPS project supplement for research and development in the field of High Tech Systems and Materials.

The authors express their sincere gratitude to both Mathias Winter, Head of Piezo System & Drive Technology, and Dr. Ing. Simon Kapelke, Head of Piezo Fundamental Technology, from Physik Instrumente (PI) SE & Co. KG, for their invaluable collaboration in providing technical insights concerning the system and its applications.

Conflict of Interest

There are no conflicts of interest.

Data Availability Statement

The datasets generated and supporting the findings of this article are obtainable from the corresponding author upon reasonable request.

Appendices

Appendix A. Minimum-Phase-Margin Tuning Condition

Let the open loop be defined as

$$\mathcal{L}(s;\,\omega_d) = \mathcal{L}_d(s)\,C_n(s;\,\omega_d) \tag{A1}$$

where $\mathcal{L}_d(s) = G(s)C_d(s)$ is the base open-loop system and

$$C_n(s;\,\omega_d) = -\frac{\omega_d - s}{\omega_d + s} \tag{A2}$$

Assume that $\mathcal{L}_d(s)$ has two distinct 0 dB crossings at

$$|\mathcal{L}_d(j\omega_{c_1})| = 1, \quad |\mathcal{L}_d(j\omega_{c_2})| = 1, \quad \omega_{c_1} < \omega_{c_2} \tag{A3}$$

and define the base-loop phases

$$\phi_{d_1} := \arg \mathcal{L}_d(j\omega_{c_1}), \quad \phi_{d_2} := \arg \mathcal{L}_d(j\omega_{c_2}) \tag{A4}$$

Since C_n is all-pass, the crossover frequencies of $\mathcal{L}(s)$ are $\omega_{c_1}, \omega_{c_2}$ for all $\omega_d > 0$.

The phase of C_n is

$$\phi_a(\omega;\,\omega_d) := \arg C_n(j\omega;\,\omega_d) = \pi - 2\arctan\left(\frac{\omega}{\omega_d}\right) \tag{A5}$$

So, the open-loop phase at the two crossovers is

$$\begin{aligned}\phi_{L_1}(\omega_d) &= \phi_{d_1} + \pi - 2\arctan\left(\frac{\omega_{c_1}}{\omega_d}\right),\\ \phi_{L_2}(\omega_d) &= \phi_{d_2} + \pi - 2\arctan\left(\frac{\omega_{c_2}}{\omega_d}\right)\end{aligned} \tag{A6}$$

With $k \in \mathbb{Z}$, the phase bands are defined as follows:

$$\phi_{\text{low}}(k) = (2k-1)\pi, \quad \phi_{\text{up}}(k) = (2k+1)\pi \tag{A7}$$

We define generalized phase margins at the two crossings as

$$\phi_1(\omega_d;\,k) := \phi_{\text{up}}(k) - \phi_{L_1}(\omega_d) \tag{A8}$$

$$\phi_2(\omega_d;\,k) := \phi_{L_2}(\omega_d) - \phi_{\text{low}}(k) \tag{A9}$$

Using the expressions above:

$$\phi_1(\omega_d;\,k) = 2k\pi - \phi_{d_1} + 2\arctan\left(\frac{\omega_{c_1}}{\omega_d}\right) \tag{A10}$$

$$\phi_2(\omega_d;\,k) = \phi_{d_2} + 2(1-k)\pi - 2\arctan\left(\frac{\omega_{c_2}}{\omega_d}\right) \tag{A11}$$

Let $\phi_{\min} > 0$ be the desired minimum-phase margin at both crossings. The conditions

$$\phi_1(\omega_d;\,k) \geq \phi_{\min}, \quad \phi_2(\omega_d;\,k) \geq \phi_{\min} \tag{A12}$$

are equivalent to

$$2\arctan\left(\frac{\omega_{c_1}}{\omega_d}\right) \geq \Xi_1(k), \quad \Xi_1(k) := \phi_{\min} + \phi_{d_1} - 2k\pi \tag{A13}$$

$$2\arctan\left(\frac{\omega_{c_2}}{\omega_d}\right) \leq \Xi_2(k), \quad \Xi_2(k) := \phi_{d_2} + 2(1-k)\pi - \phi_{\min} \tag{A14}$$

Assuming $0 < \Xi_1(k), \Xi_2(k) < \pi$ such that $\tan(\Xi_i(k)/2)$ is positive and finite, we obtain the bounds

$$\omega_d \leq \frac{\omega_{c_1}}{\tan\big(\Xi_1(k)/2\big)}, \quad \omega_d \geq \frac{\omega_{c_2}}{\tan\big(\Xi_2(k)/2\big)} \tag{A15}$$

Hence, a sufficient condition for both generalized phase margins to satisfy $\phi_i \geq \phi_{\min}$ is

$$\frac{\omega_{c_2}}{\tan\big(\Xi_2(k)/2\big)} \leq \omega_d \leq \frac{\omega_{c_1}}{\tan\big(\Xi_1(k)/2\big)} \tag{A16}$$

Appendix B. Equal Phase-Margin Tuning Condition

We now impose the equal-margins condition

$$\phi_1(\omega_d;\,k) = \phi_2(\omega_d;\,k) \tag{B1}$$

Using the expressions above:

$$2k\pi - \phi_{d_1} + 2\arctan\left(\frac{\omega_{c_1}}{\omega_d}\right) = \phi_{d_2} + 2(1-k)\pi - 2\arctan\left(\frac{\omega_{c_2}}{\omega_d}\right) \tag{B2}$$

Rearranging,

$$\arctan\left(\frac{\omega_{c_1}}{\omega_d}\right) + \arctan\left(\frac{\omega_{c_2}}{\omega_d}\right) = B_k, \quad B_k := \frac{\phi_{d_1} + \phi_{d_2} + 2(1-2k)\pi}{2} \tag{B3}$$

Let

$$a_1 := \arctan\left(\frac{\omega_{c_1}}{\omega_d}\right), \quad a_2 := \arctan\left(\frac{\omega_{c_2}}{\omega_d}\right), \quad T_k := \tan(B_k) \tag{B4}$$

Using $\tan(a_1 + a_2) = \dfrac{\tan a_1 + \tan a_2}{1 - \tan a_1 \tan a_2}$ and $\tan a_i = \omega_{ci}/\omega_d$, we obtain

$$T_k = \frac{\omega_{c_1}/\omega_d + \omega_{c_2}/\omega_d}{1 - (\omega_{c_1}\omega_{c_2})/\omega_d^2} = \frac{\omega_d(\omega_{c_1} + \omega_{c_2})}{\omega_d^2 - \omega_{c_1}\omega_{c_2}} \tag{B5}$$

This yields the quadratic equation

$$T_k\,\omega_d^2 - (\omega_{c_1} + \omega_{c_2})\,\omega_d - T_k\,\omega_{c_1}\omega_{c_2} = 0 \tag{B6}$$

whose positive real solution

$$\omega_d = \frac{(\omega_{c_1} + \omega_{c_2}) + \sqrt{(\omega_{c_1} + \omega_{c_2})^2 + 4T_k^2\,\omega_{c_1}\omega_{c_2}}}{2T_k} \quad \text{(B7)}$$

produces equal generalized phase margins at the two crossover frequencies ω_{c_1} and ω_{c_2}. In practice, ω_d is combined with the interval in Appendix A to ensure $\phi_i \geq \phi_{\min}$.

References

[1] Fleming, A. J., and Leang, K. K., 2014, *Design, Modeling and Control of Nanopositioning Systems*, Springer, Switzerland.

[2] Korolkov, V. V., Summerfield, A., Murphy, A., Amabilino, D. B., Watanabe, K., Taniguchi, T., and Beton, P. H., 2019, "Ultra-high Resolution Imaging of Thin Films and Single Strands of Polythiophene Using Atomic Force Microscopy," Nat. Commun., **10**(1), p. 1537.

[3] Rana, M. S., Pota, H., and Petersen, I., 2014, "Performance of Sinusoidal Scanning With MPC in AFM Imaging," IEEE/ASME Trans. Mechatron., **20**(1), pp. 73–83.

[4] Maroufi, M., Bazaei, A., and Moheimani, S. R., 2014, "A High-Bandwidth MEMS Nanopositioner for On-Chip AFM: Design, Characterization, and Control," IEEE Trans. Control Syst. Technol., **23**(2), pp. 504–512.

[5] Choi, K.-B., Lee, J.-J., Kim, G.-H., and Lim, H.-J., 2011, "A Piezo-Driven Ultra-precision Stage for Alignment Process of a Contact-Type Lithography," J. Korean Soc. Manuf. Technol. Eng., **20**(6), pp. 756–760.

[6] Jung, J., and Huh, K., 2010, "Simulation Tool Design for the Two-Axis Nano Stage of Lithography Systems," Mechatronics, **20**(5), pp. 574–581.

[7] Yao, T.-F., Duenner, A., and Cullinan, M., 2017, "In-Line Metrology of Nanoscale Features in Semiconductor Manufacturing Systems," Precis. Eng., **47**, pp. 147–157.

[8] Xu, Q., and Tan, K. K., 2016, *Advanced Control of Piezoelectric Micro-/Nano-positioning Systems*, Springer, Cham, Switzerland.

[9] Wang, G., and Xu, Q., 2017, "Design and Precision Position/Force Control of a Piezo-Driven Microinjection System," IEEE/ASME Trans. Mechatron., **22**(4), pp. 1744–1754.

[10] Ru, C., Liu, X., and Sun, Y., 2016, *Nanopositioning Technologies: Fundamentals and Applications*, Springer, Switzerland.

[11] Yong, Y. K., Bhikkaji, B., and Moheimani, S. R. R., 2012, "Design, Modeling, and FPAA-Based Control of a High-Speed Atomic Force Microscope Nanopositioner," IEEE/ASME Trans. Mechatron., **18**(3), pp. 1060–1071.

[12] Yong, Y., Moheimani, S. R., Kenton, B. J., and Leang, K., 2012, "Invited Review Article: High-Speed Flexure-Guided Nanopositioning: Mechanical Design and Control Issues," Rev. Sci. Instrum., **83**(12), p. 121101.

[13] Zhang, Z., and Yan, P., 2021, "Enhanced Robust Nanopositioning Control for an X–Y Piezoelectric Stage With Sensor Delays: An Infinite Dimensional H Optimization Approach," Mechatronics, **75**, p. 102511.

[14] Fleming, A. J., 2009, "Nanopositioning System With Force Feedback for High-Performance Tracking and Vibration Control," IEEE/ASME Trans. Mechatron., **15**(3), pp. 433–447.

[15] Devasia, S., Eleftheriou, E., and Moheimani, S. R., 2007, "A Survey of Control Issues in Nanopositioning," IEEE Trans. Control Syst. Technol., **15**(5), pp. 802–823.

[16] Gu, G.-Y., Zhu, L.-M., Su, C.-Y., Ding, H., and Fatikow, S., 2014, "Modeling and Control of Piezo-actuated Nanopositioning Stages: A Survey," IEEE Trans. Autom. Sci. Eng., **13**(1), pp. 313–332.

[17] Chen, Z., Zhong, X., Shi, J., and Zhang, X., 2021, "Damping-Enabling Technologies for Broadband Control of Piezo-stages: A Survey," Annu. Rev. Control, **52**, pp. 120–134.

[18] Eielsen, A. A., Vagia, M., Gravdahl, J. T., and Pettersen, K. Y., 2013, "Damping and Tracking Control Schemes for Nanopositioning," IEEE/ASME Trans. Mechatron., **19**(2), pp. 432–444.

[19] Eielsen, A. A., Vagia, M., Gravdahl, J. T., and Pettersen, K. Y., 2013, "Fixed-Structure, Low-Order Damping and Tracking Control Schemes for Nanopositioning," IFAC Proc. Vol., **46**(5), pp. 28–36.

[20] Moon, R. J., San-Millan, A., Aleyaasin, M., Feliu, V., and Aphale, S. S., 2017, "Selection of Positive Position Feedback Controllers for Damping and Precision Positioning Applications," 17th Asia Simulation Conference, AsiaSim 2017, Melaka, Malaysia, Aug. 27–29, Springer, pp. 289–301.

[21] Li, C.-X., Gu, G.-Y., Yang, M.-J., and Zhu, L.-M., 2015, "Positive Position Feedback Based High-Speed Tracking Control of Piezo-actuated Nanopositioning Stages," 8th International Conference, ICIRA 2015, Portsmouth, UK, Aug. 24–27, Springer, pp. 689–700.

[22] Fleming, A. J., Aphale, S. S., and Moheimani, S. R., 2009, "A New Method for Robust Damping and Tracking Control of Scanning Probe Microscope Positioning Stages," IEEE Trans. Nanotechnol., **9**(4), pp. 438–448.

[23] Al-Mamun, A., Keikha, E., Bhatia, C. S., and Lee, T. H., 2013, "Integral Resonant Control for Suppression of Resonance in Piezoelectric Micro-actuator Used in Precision Servomechanism," Mechatronics, **23**(1), pp. 1–9.

[24] Ling, J., Rakotondrabe, M., Feng, Z., Ming, M., and Xiao, X., 2019, "A Robust Resonant Controller for High-Speed Scanning of Nanopositioners: Design and Implementation," IEEE Trans. Control Syst. Technol., **28**(3), pp. 1116–1123.

[25] Das, S. K., Pota, H. R., and Petersen, I. R., 2014, "A Mimo Double Resonant Controller Design for Nanopositioners," IEEE Trans. Nanotechnol., **14**(2), pp. 224–237.

[26] Bhikkaji, B., Ratnam, M., and Moheimani, S. R., 2007, "PVPF Control of Piezoelectric Tube Scanners," Sens. Actuators A, **135**(2), pp. 700–712.

[27] Li, L., Li, C.-X., Gu, G., and Zhu, L.-M., 2017, "Positive Acceleration, Velocity and Position Feedback Based Damping Control Approach for Piezo-actuated Nanopositioning Stages," Mechatronics, **47**, pp. 97–104.

[28] Babarinde, A. K., Zhu, L.-M., and Aphale, S. S., 2019, "Simultaneous Design of Positive Acceleration Velocity and Position Feedback Based Combined Damping and Tracking Control Scheme for Nanopositioners," 18th European Control Conference (ECC), Naples, Italy, June 25–28, IEEE, pp. 608–613.

[29] Natu, A., and HosseinNia, H., 2026, "Non-minimum-phase Resonant Controller for Active Damping Control: Application to Piezo-actuated Nanopositioning System," Control Eng. Pract., **169**, p. 106790.

[30] Natu, A., 2024, "Overactuation for Active Damping in Compliant Positioning Stage Using Piezoelectric Transducers," IFAC-PapersOnLine, **58**(7), pp. 269–274.

[31] Dee, N. J., Natu, A. M., and HosseinNia, S., 2025, "Active Damping Control of Higher-Order Resonance Mode in Positioning Systems: Application to Prototype Compliant Dual Positioning Stage," Mechatronics, **109**, p. 103315.

[32] Udwadia, F. E., Von Bremen, H., and Phohomsiri, P., 2007, "Time-Delayed Control Design for Active Control of Structures: Principles and Applications," Struct. Control Health Monit., **14**(1), pp. 27–61.

[33] Ruderman, M., 2023, "Time-Delay Based Output Feedback Control of Fourth-Order Oscillatory Systems," Mechatronics, **94**, p. 103015.

[34] Abdallah, C., Dorato, P., Benites-Read, J., and Byrne, R., 1993, "Delayed Positive Feedback Can Stabilize Oscillatory Systems," 1993 American Control Conference (ACC), San Francisco, CA, June 2–4, IEEE, pp. 3106–3107.

[35] Koulas, M., Gutierrez, A. B., Aphale, S. S., and San-Millan, A., 2024, "Butterworth Pattern-Based Integral Resonant Controller Design for Nanopositioning Systems With Internal Delay," 2024 UKACC 14th International Conference on Control (CONTROL), Winchester, UK, Apr. 10–12, IEEE, pp. 151–156.

[36] San-Millan, A., Feliu-Batlle, V., and Aphale, S. S., 2018, "Fractional Order Implementation of Integral Resonant Control—A Nanopositioning Application," ISA Trans., **82**, pp. 223–231.

[37] San-Millan, A., Russell, D., Feliu, V., and Aphale, S. S., 2015, "A Modified Positive Velocity and Position Feedback Scheme With Delay Compensation for Improved Nanopositioning Performance," Smart Mater. Struct., **24**(7), p. 075021.

[38] Paul, A., Küçükdemiral, I., and Bevan, G., 2023, "Improving Positioning Performance of Positive Position Feedback Scheme With Delay Compensation," 2023 9th International Conference on Control, Decision and Information Technologies (CoDIT 2023) , Rome, Italy, July 3–6, IEEE, pp. 809–815.

[39] Kim, S.-M., and Brennan, M. J., 2013, "Active Vibration Control Using Delayed Resonant Feedback," Smart Mater. Struct., **22**(9), p. 095013.

[40] Kaczmarek, M. B., and HosseinNia, H., 2023, "Fractional-Order Negative Position Feedback for Vibration Attenuation," Fractal Fract., **7**(3), p. 222.